applied sciences

MDPI

Article

Lung's Segmentation Using Context-Aware Regressive Conditional GAN

Zakir Khan [1], Arif Iqbal Umar [1], Syed Hamad Shirazi [1], Assad Rasheed [1], Waqas Yousaf [1,*], Muhammad Assam [2], Izaz Hassan [2] and Abdullah Mohamed [3]

[1] Department of CS & IT, Hazara University Mansehra, Mansehra 21120, Pakistan; zakirk2012@gmail.com (Z.K.); arifiqbalumar@yahoo.com (A.I.U.); syedhamad@hu.edu.pk (S.H.S.); assad.mscs@gmail.com (A.R.)
[2] Department of Software Engineering, University of Science and Technology Bannu, Bannu 28100, Pakistan; soft.researcher12@gmail.com (M.A.); izaz.hassan88@gmail.com (I.H.)
[3] Research Centre, Future University in Egypt, New Cairo 11835, Egypt; mohamed.a@fue.edu.eg
* Correspondence: waqas21140@gmail.com

Abstract: After declaring COVID-19 pneumonia as a pandemic, researchers promptly advanced to seek solutions for patients fighting this fatal disease. Computed tomography (CT) scans offer valuable insight into how COVID-19 infection affects the lungs. Analysis of CT scans is very significant, especially when physicians are striving for quick solutions. This study successfully segmented lung infection due to COVID-19 and provided a physician with a quantitative analysis of the condition. COVID-19 lesions often occur near and over parenchyma walls, which are denser and exhibit lower contrast than the tissues outside the parenchyma. We applied Adoptive Wallis and Gaussian filter alternatively to regulate the outlining of the lungs and lesions near the parenchyma. We proposed a context-aware conditional generative adversarial network (CGAN) with gradient penalty and spectral normalization for automatic segmentation of lungs and lesion segmentation. The proposed CGAN implements higher-order statistics when compared to traditional deep-learning models. The proposed CGAN produced promising results for lung segmentation. Similarly, CGAN has shown outstanding results for COVID-19 lesions segmentation with an accuracy of 99.91%, DSC of 92.91%, and AJC of 92.91%. Moreover, we achieved an accuracy of 99.87%, DSC of 96.77%, and AJC of 95.59% for lung segmentation. Additionally, the suggested network attained a sensitivity of 100%, 81.02%, 76.45%, and 99.01%, respectively, for critical, severe, moderate, and mild infection severity levels. The proposed model outperformed state-of-the-art techniques for the COVID-19 segmentation and detection cases.

Keywords: generative adversarial network (GAN); COVID-19; lung segmentation; deep learning

Citation: Khan, Z.; Umar, A.I.; Shirazi, S.H.; Rasheed, A.; Yousaf, W.; Assam, M.; Hassan, I.; Mohamed, A. Lung's Segmentation Using Context-Aware Regressive Conditional GAN. *Appl. Sci.* **2022**, *12*, 5768. https://doi.org/10.3390/app12125768

Academic Editors: Hyo Jong Lee and Yong Yang

Received: 12 April 2022
Accepted: 2 June 2022
Published: 7 June 2022

1. Introduction

The coronavirus disease 2019 (COVID-19) has spread worldwide, affecting every area of human life. More than 200 M confirmed cases and 4.25 M deaths have been reported as of 8 August 2021, and the infection rate is still on the rise globally. Hence, precise diagnostic and effective treatment regimens are required. COVID-19 is diagnosed using a variety of methods, including isothermal nucleic acid amplification technology and real-time reverse transcription-polymerase chain reaction (RT-PCR) [1,2]. Currently, RT-PCR is extensively used to diagnose COVID-19, but it has many drawbacks such as low sensitivity, scarcity of test kits, and low efficiency [3]. Recent studies show that chest computed tomography (CT) images could be an alternative solution with higher sensitivity, accuracy, and easy accessibility in the healthcare setting.

Furthermore, CT scans of the lungs can reveal early lesions and be utilized by radiologists for diagnosis. Segmentation of the lungs is the first step to assessing lung diseases through medical imaging. Precise segmentation of infections from CT imaging is critical for

analyzing and quantifying COVID-19. There are different types of lung segmentation methods proposed by researchers, which are divided into two categories, i.e., handcrafted and deep-learning methods. Handcrafted image segmentation methods such as morphological-based methods [4] and active counter model [5] need physician intervention, are biased, and are time-consuming. These processes are often carried out in a sequence of steps, where empirical parameter adjustments are made manually. Various 3D-based [6] and 2D-based techniques [4] have been devised to obtain the best quality results. Moreover, handcrafted segmentation methods are tailored to specific imaging modalities, applications, and even datasets. It is arduous to generalize various types of imaging modalities and applications. Therefore, automatic segmentation of lung infections due to COVID-19 is highly desired in healthcare settings.

Earlier deep-learning models were based on bounding boxes [7]. The goal is to guess the central pixel(s) class label through the patch that includes its neighbors. In the field of medical image processing, numerous successful pixel-wise classification approaches based on deep learning have been designed. Ref. [8] developed a deep-learning model to segment breast and mammographic risk scoring density. Ref. [9] created a fully connected architecture for the semantic segmentation of images. Ref. [10] proposed a deep-learning-based architecture viz. segCaps for the segmentation of lung. They introduced the concept of the deconvolutional capsule in their model.

Recently, a lot of efforts have been made to design a deep-learning-based model to assist rapid and precise diagnosis of COVID-19 through medical imaging [11–13]. For example, ref. [14] developed a deep-learning architecture viz. VB-Net to segment lung infection and lung lobes from CT images of a COVID-19 Patient. Ref. [15] proposed a CT-imaging-based multi-task deep-learning architecture for the segmentation of lung infections. Ref. [16] designed mining, a lightweight deep-learning model to overcome the problem of overfitting and high computation cost. However, segmentation of lung infection due to COVID-19 accurately remains a tough job owing to three primary reasons, including: (1) the surrounding normal regions tissues and infected areas have blurry boundaries due to low contrast, which limits the accuracy of the models. (2) Large variations in shape and size induce significant challenges for precise segmentation of infectious areas of the lungs. (3) Scarcity of labeled data limits the performance of the models that depend on a large amount of data.

To tackle the problem of significant infection variations and low contrast boundaries, we have proposed a context-aware conditional generative adversarial network (CGAN) to segment infectious regions from the lungs. The proposed CGAN was trained using gradient penalty and spectral normalization. We have employed the adversarial terms in training, which foist higher-order spatial consistency instead of spatial contiguity. We presumed the problem of lung and lesions segmentation as regression instead of classification in which loss function was learned during the process of training. The suggested CGAN was evaluated on four different publicly available datasets. The rest of the manuscript is organized as follows: Section 2 summarizes the previous efforts, Section 3 describes the architecture of the proposed CGAN, training, and testing schemes, and Section 4 discusses experiments and evaluation metrics. Analysis of results and discussion are given in Section 5, and finally, Section 6 concludes this work.

2. Related Work

Recognition of COVID-19 from other kinds of pneumonia is very challenging compared to other lung problems due to high intra-class similarities (particularly in early stages) and low inter-class variations. Deep learning algorithms have a surge in popularity due to standout performance in medical image analysis. Recently, numerous studies have been conducted based on machine learning for the diagnosis of COVID-19 through CT images [11–13] and several of these representative studies are summarized in this article. Prior research studies focused on two classes, i.e., multi-class and binary classification. Multi-class identification detected COVID-19 cases from pneumonia cases, other lung

problems, and normal cases. Researchers made strenuous efforts to classify COVID-19 cases from non-COVID-19 issues in binary classification. In this research, we aim to classify COVID-19 patients from non-COVID-19 patients.

Harmon et al. [17] implemented AH-Net and several other state-of-the-art deep-learning models to locate lung parenchyma, subsequently recognizing COVID-19 infection from CT images. They used a diverse dataset consisting of 2587 lung infection CT scans. The dataset consists of 1695 non-COVID-19 cases and 922 COVID-19 cases. AH-Net achieved a segmentation accuracy of 95%, while 3D-Densnet-121 was employed to identify COVID-19 and non-COVID-19 infection and achieved a discriminative accuracy of 88.9%. Zhou et al. [18] designed a lesion identification framework to quantify the area affected by COVID-19. They used lung CT images. Three separate 2-D UNet were implemented for X-Y, X-Z, and Y-Z views of the CT image, each with five neighboring slices as an input and a central portion as an infection prediction mask. The proposed model achieved a sensitivity of 77.6% and a DSC score of 78.3%.

Wang et al. [19] developed a semi-supervised deep-learning-based model for the localization and classification of COVID-19. Firstly, the segmentation of the infectious regions was carried out through the help of a pre-trained UNet. Secondly, a deep CNN was employed to classify the lung region to COVID-19 or not. They used a dataset consisting of 313 images of COVID-19 and 229 images of non-COVID-19 cases. They obtained a classification accuracy of 0.95% and a 0.976% precision score. However, 68.5% of HR (hit rate) recorded a low segmentation result.

Mei et al. [20] designed a joint framework to integrate the clinical findings such as exposure history, symptoms, and lab tests with CT images to classify COVID-19 and non-COVID-19 cases. They trained a joint framework with the help of a dataset consisting of 905 cases. They achieved a specificity of 82.8%, sensitivity of 84.3%, and 0.92% AUC (area under the curve) values. Chaganti et al. [21] developed a model for the segmentation and quantification of aberrant patterns on lung CT scans of COVID-19 cases. They used 9749 lung CT scans, segmented lesions, and lobe regions. They employed different evaluation matrices to quantify severity: % of opacity, % of high opacity, severity score, etc. Pu et al. [22] developed an automatic approach to measure COVID-19 pneumonia progression and severity. UNet was employed to segment lungs and vessels through 120 CT images of COVID-19 patients. For the segmentation of lesions, the proposed method obtained a DSC score of 81% and 95% for the segmentation of lung regions. Shen et al. [23] designed a framework to determine the severity of COVID-19 pneumonia. The developed framework consists of four stages, i.e., pulmonary vessels segmentation, lung segmentation, and lobes segmentation and infection detection. The segmentation was performed using adaptive region growing and thresholds. The Pearson correlation between physician and computer ranged from 0.8373 to 0.7679.

Sahlol et al. [24] created a hybrid classification model that combines an improved PSO (particle swarm optimization) and a deep CNN model. The aim was to achieve high performance with minimum resource utilization and storage capacity. They employed a novel and efficient feature optimizer viz. fractional-order marine predator algorithm to choose the best features from a huge feature vector extracted via CNN. The results revealed the supremacy of the proposed method over existing techniques for the said problem.

Notwithstanding the substantial amount of work on lesion recognition, detection of a specific type of lesion from COVID-19 through images is still challenging. Earlier studies aimed to distinguish lesions using CT scans. Most of the previous studies applied UNet to segment lesions through computed tomographic images [25], Li et al. [26] differentiated COVID-19 from community-acquired pneumonia, and Huang et al. [27] and Cao et al. [28] extracted pulmonary opacities in the lung's CT scans for quantitative assessment. All of these techniques need precise annotation of lesions for training purposes.

3. Materials and Methods

Ian Goodfellow created GAN consisting of two adversarial sub-networks, i.e., generator and discriminator. GANs based models are very prominent in research communities, and there are various variants of GANs such as conditional GAN, super-resolution GAN, vanilla GAN, etc. The generator and discriminator networks compete against each other during training. The generator seeks to determine the data distribution while the discriminator attempts to estimate the probability of input data. Both the generator and the discriminator needed to be trained at the same time, and both required parameter adjustments to reduce the log $(1 - d(g(z)))$, and logdx. The generator network G seeks to maximize its loss, while the discriminator network strives to minimize its reward $(d,\ g)$. This minimax process is mathematically represented in Equation (1) below.

$$min_G\ max_D V(D,\ G) = E_{x\sim p_i(x)}[\log d(x)] + E_{z\sim p_z(z)}[\log(1 - d(g(z)))] \quad (1)$$

where G stands for Generator and D for the discriminator, V (D, G) denotes value function, x represents data, and p_i and p_z means data and prior noise distribution. We have designed a conditional GAN derived from empirical knowledge from the widely used GAN.

3.1. Conditional GAN for Lesions and Lungs Segmentation

One of the biggest problems in the segmentation of lungs and lesions is the identification of boundaries. Conventional deep-learning methods depend upon the depreciation of pixel-wise loss. The role of a misclassified pixel is not prominent for the overall loss but can eventually lead to the segmentation of multiple lungs regions as one. Such kinds of challenges could be tackled by distance map regression [29], concave point identification [30], and contour prediction [31]. CRFs (conditional random fields) have been widely employed [32]. CNN-CRF is also used for context-aware training of models [33].

Notwithstanding the advancement in CNN-CRF networks, this technique is restricted to unary or pairwise CRFs, which embody only lower-order statistics. According to [32], higher-order statistics benefit medical image segmentation. Similarly, adversarial training permits higher-order potential without restricting a specific type of higher-order consistency and has field-of-view instead of pixel-wise.

The adversarial model can learn a suitable loss function that avoids manually concocted loss functions. This mechanism has also been explained extensively in [34]. These models can identify small changes in a range of higher-order consistencies between ground-truth and predicted segmentation masks. The suggested conditional GAN learns a mapping m for lung segmentation, in which m can acclimate lung images to their segmentation masks. To train the proposed model with pair data for segmentation, the CGAN objective function encompasses an adversarial loss function F_l and pixel-wise loss function L_1 to reprimand segmentation errors. The loss in conditional GANs is analogous to cycle-GAN, in which the segmentation network S_n and discriminator D_n play a minimax game in minimizing and maximizing the objective, $mini_{S_n} max_{D_n} F_l(S_n,\ D_n)$. Explicitly, S_n interprets lung CT scans to realistic masks to reduce cross-entropy loss of D_n. The adversarial loss can be construed as structured loss, in which S_n is reprimanded if pixels in the predicted masks are unrealistic. The objective of the proposed model is expressed as in Equation (2).

$$\begin{aligned} F_l(S_n, D_n) = \quad & \mathbb{E}_{m,\ n\sim p_{data}(m,n)}[\log D_m(m,n)] \\ & +\mathbb{E}_{n\sim p_{data}(n)}[\log(1 - D_m(m,\ S_n(n)))] \end{aligned} \quad (2)$$

where m represent masks and n denotes lung lesion images. For stabilization of training and bringing prediction closer to the ground truth, we have employed the addition loss function L_1 as Equation (3).

$$L_1(S_n) = \mathbb{E}_{n=m,\ n\sim P_{data}(m,\ n)}[\|\ m - S_n(n)\ \|_1] \quad (3)$$

3.2. Architecture Detail

The GAN architecture comprises the Generator sub-network and discriminator sub-network, as shown in Figure 1. The very popular conditional GAN inspires it. The network should produce an estimated output from input representation, i.e., COVID-19 image. The generator sub-network has two functionally constrained convolutions with strides of size $1/2$, two strides-2 convolutions, and twelve residual blocks. To minimize artifacts, the concept of reflection padding is used. The discriminator sub-network is a simple classification architecture consisting of three layers and an output layer of 70×70 size to predict whether or not the overlapping patches are real. The discriminator is a patch-level structure with fewer parameters and is suitable for various size images. However, numerous residual blocks are required for efficient convergence in the case of larger-size images. To normalize the training process, spectral normalization is implemented in this model.

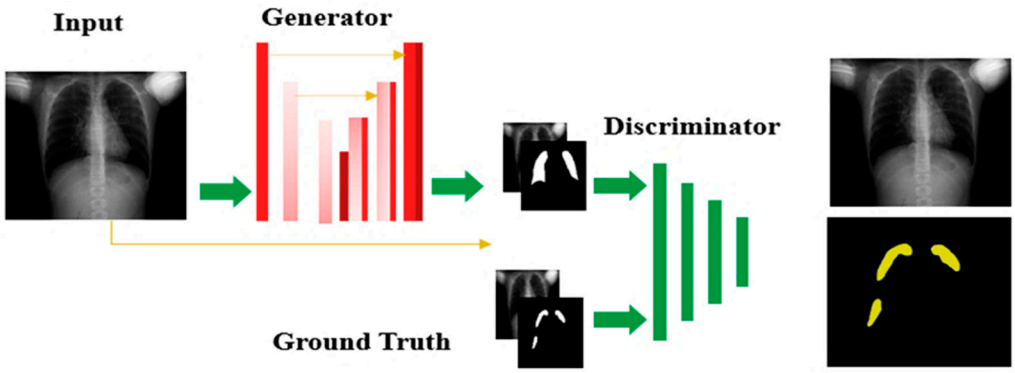

Figure 1. Structure of the proposed CGAN.

3.3. Training Details

We evaluated the performance of the proposed CGAN model on four different lung lesion datasets. For a fair comparison, we implemented benchmark image segmentation models. Finally, we implemented the proposed CGAN architecture to solve the problem of lung infection segmentation, demonstrating the benefits of the proposed model. Training begins by feeding annotated lung lesions images. The Adam optimizer was set for 170 epochs and the decay to 0 for the remaining epochs (total 380 epochs) to solve objective loss. A batch size of 1 and a learning rate of 0.0002 were set. We trained the model from scratch, and a standard deviation of 0.02 and mean of 0 of Gaussian distribution were employed to initialize weight. The training was performed using PyTorch deep learning library version V.0.4.0, with NVIDIA 1050Ti 4GB GPU (Graphics processing unit). Since the goal of the proposed model was to design a distinct generator network, the objective function was divided by 2 for the optimization of the discriminator. Spectral normalization [35] was adopted to enhance the GAN training stability.

The training of the proposed CGAN for lung segmentation lasted for approximately 6 minutes per epoch and approximately 5 min for lesion segmentation on our system. The inference time per image was recorded at approximately 20 s for lesion and lung segmentation for CGAN as shown in Table 1.

3.4. Lung and Lesions Segmentation

An encoder–decoder network was implemented to segment the affected region of the lungs from CT images. Skip connections are used in the generator between the nth and n -mth layer. Each skip connection in the encoder–decoder in the generator simply combines the corresponding layers. A convolutional layer is added to the map output segmentation mask at the decoder's end, followed by the tanh activation function. We used Leaky-ReLU (Rectified linear unit) activation function with a slope of 0.2 in the encoder and simple ReLU in the decoder network. Discriminator also used leaky ReLU with a slope of 0.2.

Table 1. List the time taken by employed models for this task.

Method	Training Time Lungs Segmentation	Training Time Lesion Segmentation	Inference Time per Image
UNet	6 min	5 min	17 s
FCN	5 min	4 min	13 s
Mask-RCNN	7 min	5 min	17 s
UNet+ FCN	7 min	6 min	19 s
UNet+ Mask-RCNN	8 min	7 min	22 s
UNet+ FCN+ Mask-RCNN	9 min	7 min	28 s
GAN	6 min	5 min	19 s
Proposed CGAN	6 min	5 min	20 s

4. Experiments

4.1. Datasets

This study utilized four publicly available datasets from various sources to train and assess the proposed CGAN. This work used 907 patients and 5726 CT slices. The following Table 2 shows a list of the datasets that were used: the first dataset consists of 3520 CT images with COVID-19 infections rates in the lungs ranging from 0.1 percent to 59 percent. These images were precisely annotated and verified by radiologists. The second dataset is the "COVID-19 CT segmentation dataset", ref. [36] based on Radiopaedia volumetric CTs. It is composed of 829 slices from 20 patients. The third dataset [37] consists of 267 CT slices and their relevant ground-truth masks. This dataset consists of lung CT images with non-COVID-19 cases. Moreover, the MosMedData [38] dataset was utilized for external validation. The dataset was collected between 1 March and 25 April 2020, and comprises 1110 CT slices. The dataset includes 856 COVID-19 cases and 254 normal cases. The COVID-19 cases are divided into four categories, i.e., CTI (684 CT images, 1–25% lungs infection), CT2 (125 images, lung's infection ranging from 25–50%), CT3 (45 images, infection percentage ranges from 50–75%) and CT4 (2 CT images, infection percentage ranging from 75% and higher).

Table 2. Description of datasets employed in this study.

Dataset	No. of Patients	CT Images
COVID-19 CT Lung and Infection Segmentation Dataset	20	3520
MosMedData	856	1110
COVID-19 CT segmentation dataset	20	829
CT Data (Kaggle)	11	267

4.2. Preprocessing

Segmentation of lungs produces inconsistency near the lungs contour. COVID-19 lesions predominantly occur over the parenchyma walls, which are denser and exhibit lower contrast than the tissues outside the parenchyma. An adoptive Wallis filter and Gaussian filter are used to regulate the outlining of the lungs. This process is repeated until an improved resultant image produces as shown in Figure 2 below. All the datasets used in this study have images in neuroimaging informatics technology initiative (NITI) format except CT data (Kaggle) which introduced inconsistency among features across various datasets. We have converted all the images into PNG format and normalized the pixel values within the 0–254 range to reduce inconsistencies. In the end, all the images from four datasets were resized to 256 × 256.

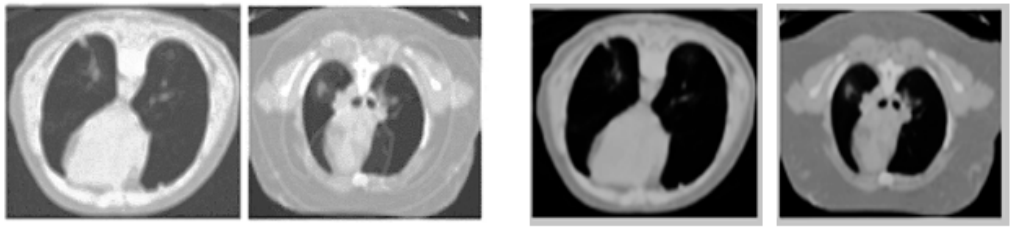

(**a**) Original Images (**b**) Processed Images

Figure 2. Shows unprocessed (original images) and processed lung CT scans.

4.3. Data Augmentation

To tackle the data imbalance problem, which might lead to subsequent overfitting, data augmentation was performed to equalize the number of CT images in each class of the datasets. We have applied −90, 90, and 180-degree rotation for ground-truth and CT scans. The number of images in each dataset used for training, validation, and testing of the proposed model is listed in Table 3 below. The proposed CGAN was trained via a 5-fold cross-validation scheme where 60% of the data were used for training, 20% for validation, and the remaining 20% for testing.

Table 3. Shows the total number of original and augmented images used to train and evaluate the proposed CGAN.

No of CT Images	Lung Segmentation	Lesion Segmentation
Total CT images	4616	3520
Training images	2955	2553
Augmented training images	11,820	9012
Validation images	923	563
Test images	738	704

4.4. Evaluation Metrics

We have employed the most commonly used and accepted metrics for image segmentation problems. Three different evaluation metrics, i.e., Accuracy, Dice similarity coefficient (DSC), and intersection over union (IoU), were used to judge output quality empirically.

4.4.1. Accuracy

Accuracy refers to the ratio of accurate classification of pixels among the pixels of an image. Mathematically shown in Equation (4) below:

$$\text{Accuracy} = \frac{\text{True positive} + \text{True Negative}}{\text{True positive} + \text{True Negative} + \text{False positve} + \text{False Negative}} \quad (4)$$

4.4.2. Aggregated Jaccard Coefficient

The aggregated Jaccard coefficient/index is a quantitative assessment used for analyzing the similarities and differences of sample sets. It extends the global Jaccard coefficient that is used to gauge aggregated intersection and aggregated union cardinality in the ROI (region of interest). The mathematical dynamics of this concept are illustrated in the following Equation (5) below.

$$J_{jac} = \frac{\sum_{i=1}^{I} \left| T_i \cap P_J^*(i) \right|}{\sum_{i=1}^{k} \left| T_i \cup P_J^*(i) \right| + \left| \sum_{k \in U} IP_k \right|} \quad (5)$$

where $T = U_{i=1,2,3,...k}$, T_i denote ground-truth. $P = U_{i=1,2,3,....k}$ Prediction and $P_J^*(i)$ indicates connected components. More significant values of the Jaccard coefficient specify better results of the applied method. The values calculated for the proposed model for lung segmentation and lesion segmentation are shown in Tables 4 and 5.

Table 4. Lung segmentation results using state-of-the-art deep-learning models and proposed CGAN.

Model	Accuracy (%)	Aggregated Jaccard Coefficient (%)	DSC (%)
UNet	99.68	95.01	96.57
FCN	94.44	89.76	95.99
Mask-RCNN	99.43	95.21	96.62
UNet+ FCN	99.69	95.02	96.58
UNet+ Mask-RCNN	99.72	95.23	96.66
UNet+ FCN+ Mask-RCNN	99.73	95.27	96.70
GAN	99.54	95.34	96.65
Proposed CGAN	99.87	95.59	96.77

Table 5. Lists the results of lesion segmentation.

Model	Accuracy (%)	Aggregated Jaccard Coefficient (%)	DSC (%)
UNet	99.81	90.07	92.43
FCN	93.56	89.17	92.82
Mask-RCNN	99.80	90.25	92.53
UNet+ FCN	99.81	90.09	92.47
UNet+ Mask-RCNN	99.83	92.26	92.55
UNet+ FCN+ Mask-RCNN	99.84	91.28	92.57
GAN	99.82	91.18	92.60
Proposed CGAN	99.91	92.03	92.91

4.4.3. Dice Similarity Coefficient (DSC)

DSC is a statistical method used to gauge spatial overlap between predicted and ground-truth masks. Mathematically it is represented in Equation (6).

$$\text{DSC} = \frac{2(TP)}{2(TP) + FN + FP} \tag{6}$$

4.4.4. F1 Score

It is the harmonic mean of precision and recall. Mathematically, it is computed as in the following Equation (7).

$$F_1 = \frac{\text{Recall} \times \text{precision}}{\text{Recall} + \text{precison}} \tag{7}$$

A high score of F_1 indicates better performance of the applied method. F_1 score for the problem of lung infection segmentation is demonstrated in Table 6.

Table 6. Shows classification COVID-19 severity levels.

Severity Level	Infection (%)	Accuracy	Sensitivity	Specificity	F1-Score
Cr	76–100%	100%	100%	100%	100%
ST	51–75%	98.63%	81.02%	98.77%	72.26%
MT	26–50%	96.29%	76.45%	98.94%	80.61%
mT	1–25%	97.32%	99.01%	94.11%	98.23%
HT	0% (Healthy)	99.10%	96.21%	98.51%	98.71%

5. Results and Discussion

This section of the article illustrates the results of the lesion and lung segmentation, severity estimation, and COVID-19 detection.

5.1. Lung Segmentation

The performance of the proposed CGAN and state-of-the-art segmentation models is shown in Table 4. It is noticed that UNet, Mask-RCNN, and GAN are the top-performers for the segmentation of lungs. However, it is shown that the FCN model did not perform well compared to the UNet network, which is state-of-the-art architecture for segmentation tasks. Mask-RCNN has indicated the acceptable DSC score for the segmentation of lungs. The proposed CGAN is the top-performer network for the segmentation of lungs with DSC and AJC of 96.77% and 95.59%, respectively. It has been observed that the top-three performers have very successfully segmented the tiny areas from the lung regions, as illustrated in Table 4. Even though the lungs are badly affected by COVID-19, the trained model could segment the lungs' boundaries correctly, as reflected in Figure 3, which highlights the robustness of the suggested lung segmentation model in this work. To further improve the performance of the applied CNN models, we have ensembled UNet+ FCN, UNet+ Mask-RCNN, and UNet+ FCN+ Mask-RCNN. We noticed a minute improvement in the performance, as listed in Table 4.

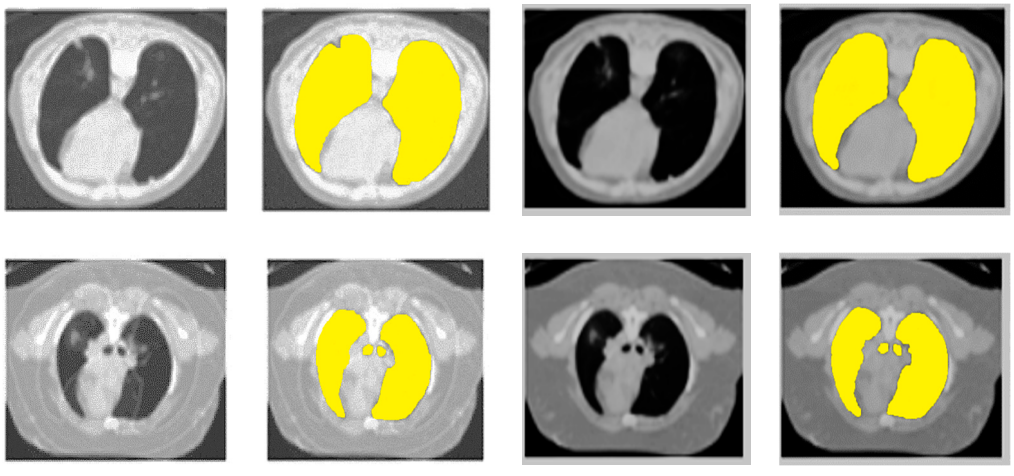

Figure 3. Results of lung segmentation using proposed CGAN before (**b**) and after (**d**) preprocessing. (**a**–**d**) Preprocessing enables models to segment lungs regions robustly and ignore other regions along the boundary lines i.e., reflections, noise etc.

In this research, various preprocessing steps were performed to enable us to assess the networks on the different datasets and utilize only slices where the lungs are visible. Segmentation of the lungs is conducted as part of the pre-processing. This procedure proved very effective in our preliminary experiments. We have demonstrated how the proposed method enhances performance by improving the stability of CGAN during training. We have implemented the proposed CGAN with the initial batch normalization

setting instead of spectral normalization. A learning rate of 0.002 caused oscillation during training, and worse results are noted for CGAN. The initial GAN setting utilized crop entropy loss function and suffered from collapse; to avoid this, we have adopted the mechanism suggested by [34].

5.2. Lesion Segmentation

The presence of vessels during the lesion segmentation obstructs the process of circumvention by the expert and also makes the training of an automatic model very difficult. For the robust training of the model, these vessels are required to be excluded. Therefore, these vessels are first segmented and then extracted from the marking of the experts. The segmentation of vessels was performed using the proposed CGAN, subsequently to segmentation of the lesion.

The segmentation results of various models are shown in Table 5. The results show that CGAN is more consistent with the ground truth than UNet and GAN. The proposed CGAN obtained better segmentation results than the benchmarking segmentation models. CGAN obtained the best results with DSC of 92.91% and AJC of 92.03%. Mask-RCNN, UNet, and GAN's results are close to the proposed CGAN model with minimal differences. Figure 4 presents segmented tiny lung regions with the help of proposed CGAN and other state-of-the-art deep-learning models. The results of the state-of-art segmentation models are presented in Figure 4. It is evident from Figure 4 that the segmentation result of CGAN, GAN, Mask-RCNN, and UNet is highly congruent with the ground truth.

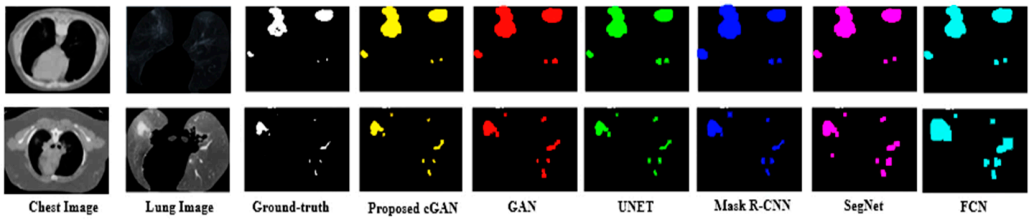

Figure 4. Lesion segmentation using state-of-the-art deep-learning models and proposed CGAN.

5.3. COVID-19 Detection

COVID-19 was detected using prediction maps produced by the lesion segmentation model. Consequently, a CT slice was classed as positive if at least one pixel was anticipated to be infected with COVID-19, that is, softmax probability >0.5; otherwise, the image was deemed negative that is normal. The severity levels of COVID-19 infection are divided into four categories, i.e., severe, critical, mild, and healthy, on the basis of average infection percentage (white pixels over the lungs regions) all the CT slices of the entire volume.

Table 6 shows the performance of lesion segmentation by the different models used in this work. We have considered sensitivity as the primary metric for the detection of COVID-19. All the models obtained the best sensitivity score where CGAN achieved the highest sensitivity of 99.93%, which indicates the robustness of the proposed model. Furthermore, C obtained a specificity value of 98.5% which is an indication of a low false alarm rate.

5.4. COVID-19 Severity Classification

The MosMedData dataset was used for the classification of severity levels in this study. The ground truth for the task under review is already provided in this dataset. We have segmented the lungs and infection regions using CGAN that proved to be the best for detecting borders from CT Volumes more precisely than others, as shown in Figure 4. The percentage of infection for each lung CT volume is calculated, where each volume is categorized as severe (ST), critical (Cr), moderate (MT), mild (mT), or healthy (HT). The classification and quantification of severity levels are shown in Table 6 above. We have considered sensitivity as the primary metric for the detection of COVID-19. All the models obtained the best sensitivity score where CGAN achieved the highest sensitivity of 99.93%, which indicates the robustness

of the proposed model. Furthermore, C obtained a specificity value of 98.5% which is an indication of a low false alarm rate. The proposed model can identify Cr with 100% accuracy according to the confusion matrix. Furthermore, a high percentage of normal cases (HT) were determined accurately. Only ten instances were misclassified, whereas six out of ten cases exhibited a low infection ratio of 2–4%. Notwithstanding that, the MosMedData Dataset description stated no viral pneumonia for (HT) cases. Other pulmonary disorders may be detected in HT cases. All COVID-19 pneumonia cases were identified as ST, MT, mT except HT. Figure 5 presents a few of the COVID-19 predicted cases. Moreover, the proposed model has shown a low sensitivity rate for ST, mT compared to HT and MT. This might be linked to the labeling of the dataset through visual semi-quantitative techniques by the radiologist.

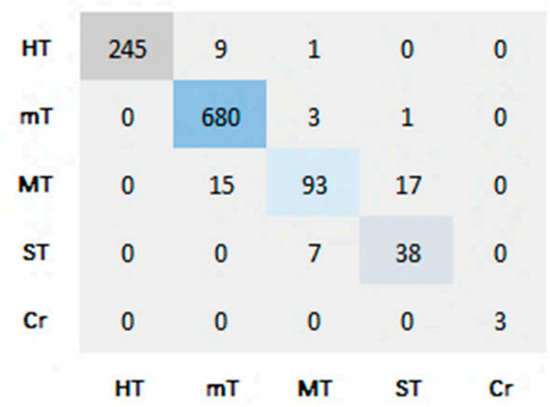

Figure 5. Severity classification confusion matrix.

6. Conclusions

In this study, we have proposed a GAN-based network for lung lesion segmentation and quantification of infection severity levels. Various benchmarked deep-learning models were also evaluated to determine the most suitable segmentation model for this task. The proposed CGAN outperformed all of them to segment lesions and lungs. We have classified different severity levels based on segmented infected lung regions. The critical contribution of this work is as follows. For lesion and lung segmentation, the proposed CGAN outperformed best performing models for such types of task. The proposed CGAN achieved 99.87% and 99.63% accuracy for the segmentation of lungs and infected regions, i.e., lesions, respectively. The proposed model achieved an accuracy of 99.63% for the detection of COVID-19. We classified the severity of COVID-19 infection into levels (critical, severe, moderate, and mild) based on the percentage of disease by using the segmentation output of the proposed model. The system achieved a sensitivity of 100%, 81.02%, 76.45%, 99.01% for critical, severe, moderate, and mild infections. In short, the proposed computer-aided identification and quantification system is a simple, efficient, and accurate prospect to diagnose COVID-19 cases. The proposed method learns the loss function by considering the entire image instead of pixel-wise loss. This approach makes them contextually aware and globally more consistent. The proposed CGAN needs extensive data for effective training and may suffer from inconsistency during training.

Author Contributions: Z.K., A.I.U. and S.H.S. conceived the overall concept and formulated the study designs. A.R. and M.A. wrote the paper and performed data analysis. Z.K. and W.Y. wrote code and performed computational experiments. I.H. and A.M. rectified the paper and tuned the network for robust results. All authors have read and agreed to the published version of the manuscript.

Funding: This research received no external funding.

Institutional Review Board Statement: Not applicable.

Informed Consent Statement: Not applicable.

Conflicts of Interest: The authors declare no conflict of interest.

References

1. Craw, P.; Balachandran, W. Isothermal nucleic acid amplification technologies for point-of-care diagnostics: A critical review. *Lab. Chip.* **2012**, *12*, 2469–2486. [CrossRef]
2. Corman, V.M.; Landt, O.; Kaiser, M.; Molenkamp, R.; Meijer, A.; Chu, D.K.W.; Bleicker, T.; Brünink, S.; Schneider, J.; Schmidt, M.L.; et al. Detection of 2019 novel coronavirus (2019-nCoV) by real-time RT-PCR. *Eurosurveillance* **2020**, *25*, 2000045. [CrossRef]
3. Kakodkar, P.; Kaka, N.; Baig, M. A Comprehensive Literature Review on the Clinical Presentation, and Management of the Pandemic Coronavirus Disease 2019 (COVID-19). *Cureus* **2020**, *12*, e7560. [CrossRef] [PubMed]
4. Mansoor, A.; Bagci, U.; Foster, B.; Xu, Z.; Papadakis, G.Z.; Folio, L.R.; Udupa, J.K.; Mollura, D.J. Segmentation and Image Analysis of Abnormal Lungs at CT: Current Approaches, Challenges, and Future Trends. *RadioGraphics* **2015**, *35*, 1056–1076. [CrossRef]
5. Kass, M.; Witkin, A.; Terzopoulos, D. Snakes: Active contour models. *Int. J. Comput. Vis.* **1988**, *1*, 321–331. [CrossRef]
6. Sun, S.; Bauer, C.; Beichel, R. Automated 3-D Segmentation of Lungs with Lung Cancer in CT Data Using a Novel Robust Active Shape Model Approach. *IEEE Trans. Med Imaging* **2011**, *31*, 449–460. [CrossRef]
7. Tan, J.; Huo, Y.; Liang, Z.; Li, L. Apply Convolutional Neural Network to Lung Nodule Detection: Recent Progress and Challenges. In *International Conference on Smart Health*; Springer: Cham, Switzerland, 2017; pp. 214–222.
8. Kallenberg, M.; Petersen, K.; Nielsen, M.; Ng, A.Y.; Diao, P.; Igel, C.; Vachon, C.M.; Holland, K.; Winkel, R.R.; Karssemeijer, N.; et al. Unsupervised Deep Learning Applied to Breast Density Segmentation and Mammographic Risk Scoring. *IEEE Trans. Med Imaging* **2016**, *35*, 1322–1331. [CrossRef]
9. Long, J.; Shelhamer, E.; Darrell, T. Fully convolutional networks for semantic segmentation. In Proceedings of the IEEE Conference on Computer Vision and Pattern Recognition, Boston, MA, USA, 12 June 2015; pp. 3431–3440.
10. LaLonde, R.; Bagci, U. Capsules for object segmentation. *arXiv* **2018**, arXiv:1804.04241.
11. Xu, X.; Jiang, X.; Ma, C.; Du, P.; Li, X.; Lv, S.; Yu, L.; Chen, Y.; Su, J.; Lang, G. Deep Learning System to Screen novel Coronavirus Disease 2019 Pneumonia. *Engineering* **2020**, *6*, 1122–1129. [CrossRef]
12. Kang, H.; Xia, L.; Yan, F.; Wan, Z.; Shi, F.; Yuan, H.; Jiang, H.; Wu, D.; Sui, H.; Zhang, C.; et al. Diagnosis of Coronavirus Disease 2019 (COVID-19) With Structured Latent Multi-View Representation Learning. *IEEE Trans. Med Imaging* **2020**, *39*, 2606–2614. [CrossRef] [PubMed]
13. Fan, D.-P.; Zhou, T.; Ji, G.-P.; Zhou, Y.; Chen, G.; Fu, H.; Shen, J.; Shao, L. Inf-Net: Automatic COVID-19 Lung Infection Segmentation From CT Images. *IEEE Trans. Med. Imaging* **2020**, *39*, 2626–2637. [CrossRef]
14. Ouyang, X.; Huo, J.; Xia, L.; Shan, F.; Liu, J.; Mo, Z.; Yan, F.; Ding, Z.; Yang, Q.; Song, B.; et al. Dual-Sampling Attention Network for Diagnosis of COVID-19 From Community Acquired Pneumonia. *IEEE Trans. Med. Imaging* **2020**, *39*, 2595–2605. [CrossRef]
15. Amyar, A.; Modzelewski, R.; Li, H.; Ruan, S. Multi-task deep learning based CT imaging analysis for COVID-19 pneumonia: Classification and segmentation. *Comput. Biol. Med.* **2020**, *126*, 104037. [CrossRef]
16. Qiu, Y.; Liu, Y.; Li, S.; Xu, J. Miniseg: An extremely minimum network for efficient COVID-19 segmentation. *arXiv* **2020**, arXiv:2004.09750.
17. Harmon, S.A.; Sanford, T.H.; Xu, S.; Turkbey, E.B.; Roth, H.; Xu, Z.; Yang, D.; Myronenko, A.; Anderson, V.; Amalou, A.; et al. Artificial intelligence for the detection of COVID-19 pneumonia on chest CT using multinational datasets. *Nat. Commun.* **2020**, *11*, 4080. [CrossRef]
18. Zhou, L.; Li, Z.; Zhou, J.; Li, H.; Chen, Y.; Huang, Y.; Xie, D.; Zhao, L.; Fan, M.; Hashmi, S.; et al. A rapid, accurate and ma-chine-agnostic segmentation and quantification method for CT-based COVID-19 diagnosis. *IEEE Trans. Med. Imaging* **2020**, *39*, 2638–2652. [CrossRef]
19. Wang, X.; Deng, X.; Fu, Q.; Zhou, Q.; Feng, J.; Ma, H.; Liu, W.; Zheng, C. A weakly-supervised framework for COVID-19 classifica-tion and lesion localization from chest CT. *IEEE Trans. Med. Imaging* **2020**, *39*, 2615–2625. [CrossRef] [PubMed]
20. Mei, X.; Lee, H.-C.; Diao, K.-Y.; Huang, M.; Lin, B.; Liu, C.; Xie, Z.; Ma, Y.; Robson, P.M.; Chung, M.; et al. Artificial intelligence–enabled rapid diagnosis of patients with COVID-19. *Nat. Med.* **2020**, *26*, 1224–1228. [CrossRef] [PubMed]
21. Chaganti, S.; Grenier, P.; Balachandran, A.; Chabin, G.; Cohen, S.; Flohr, T.; Georgescu, B.; Grbic, S.; Liu, S.; Mellot, F.; et al. Au-tomated quantification of CT patterns associated with COVID-19 from chest CT. *Radiol. Artif. Intell.* **2020**, *2*, e200048. [CrossRef]
22. Pu, J.; Leader, J.K.; Bandos, A.; Ke, S.; Wang, J.; Shi, J.; Du, P.; Guo, Y.; Wenzel, S.E.; Fuhrman, C.R.; et al. Automated quantification of COVID-19 severity and progression using chest CT images. *Eur. Radiol.* **2020**, *31*, 436–446. [CrossRef] [PubMed]
23. Shen, C.; Yu, N.; Cai, S.; Zhou, J.; Sheng, J.; Liu, K.; Zhou, H.; Guo, Y.; Niu, G. Quantitative computed tomography analysis for strati-fying the severity of Coronavirus Disease 2019. *J. Pharm. Analysis.* **2020**, *10*, 123–129. [CrossRef] [PubMed]
24. Sahlol, A.T.; Yousri, D.; Ewees, A.A.; Al-Qaness, M.A.A.; Damasevicius, R.; Elaziz, M.A. COVID-19 image classification using deep features and fractional-order marine predators algorithm. *Sci. Rep.* **2020**, *10*, 15364. [CrossRef]
25. Ronneberger, O.; Fischer, P.; Brox, T. U-net: Convolutional networks for biomedical image segmentation. In Proceedings of the International Conference on Medical Image Computing and Computer-Assisted Intervention, Munich, Germany, 5–9 October 2015; Springer: Cham, Switzerland, 2015; pp. 234–241.
26. Li, L.; Qin, L.; Xu, Z.; Yin, Y.; Wang, X.; Kong, B.; Bai, J.; Lu, Y.; Fang, Z.; Song, Q.; et al. Using artificial intelligence to detect COVID-19 and community-acquired pneumonia based on pulmonary CT: Evaluation of the diagnostic accuracy. *Radiology* **2020**, *296*, E65–E71. [CrossRef]
27. Huang, L.; Han, R.; Ai, T.; Yu, P.; Kang, H.; Tao, Q.; Xia, L. Serial Quantitative Chest CT Assessment of COVID-19: A Deep Learning Approach. *Radiol. Cardiothorac. Imaging* **2020**, *2*, e200075. [CrossRef] [PubMed]

28. Cao, Y.; Xu, Z.; Feng, J.; Jin, C.; Han, X.; Wu, H.; Shi, H. Longitudinal assessment of COVID-19 using a deep learning–based quanti-tative CT pipeline: Illustration of two cases. *Radiol. Cardiothorac. Imaging* **2020**, *2*, e200082. [CrossRef]
29. Naylor, P.; Laé, M.; Reyal, F.; Walter, T. Segmentation of Nuclei in Histopathology Images by Deep Regression of the Distance Map. *IEEE Trans. Med. Imaging* **2018**, *38*, 448–459. [CrossRef]
30. Zhang, W.; Li, H. Automated segmentation of overlapped nuclei using concave point detection and segment grouping. *Pattern Recognit.* **2017**, *71*, 349–360. [CrossRef]
31. Van Valen, D.A.; Kudo, T.; Lane, K.M.; Macklin, D.N.; Quach, N.T.; DeFelice, M.M.; Maayan, I.; Tanouchi, Y.; Ashley, E.A.; Covert, M.W. Deep learning automates the quantitative analysis of individual cells in live-cell imaging experiments. *PLoS Comput. Biol.* **2016**, *12*, e1005177. [CrossRef]
32. Luc, P.; Couprie, C.; Chintala, S.; Verbeek, J. Semantic segmentation using adversarial networks. *arXiv* **2016**, arXiv:1611.08408.
33. Chen, R.; Mahmood, F.; Yuille, A.; Durr, N.J. Rethinking monocular depth estimation with adversarial training. *arXiv* **2018**, arXiv:1808.07528.
34. Isola, P.; Zhu, J.Y.; Zhou, T.; Efros, A.A. Image-to-image translation with conditional adversarial networks. In Proceedings of the IEEE Conference on Computer Vision and Pattern Recognition, Honolulu, HI, USA, 21–26 July 2017; pp. 1125–1134.
35. Miyato, T.; Kataoka, T.; Koyama, M.; Yoshida, Y. Spectral normalization for generative adversarial networks. *arXiv* **2018**, arXiv:1802.05957.
36. Yang, X.; He, X.; Zhao, J.; Zhang, Y.; Zhang, S.; Xie, P. COVID-CT-dataset: A CT scan dataset about COVID-19. *arXiv* **2020**, arXiv:2003.13865.
37. Mader, K.S. Finding and Measuring Lungs in CT Data. Available online: https://www.kaggle.com/kmader/finding-lungs-in-ctdata (accessed on 12 May 2021).
38. Morozov, S.P.; Andreychenko, A.E.; Pavlov, N.A.; Vladzymyrskyy, A.V.; Ledikhova, N.V.; Gombolevskiy, V.A.; Blokhin, I.A.; Gelezhe, P.B.; Gonchar, A.V.; Chernina, V.Y. Mosmeddata: Chest ct scans with COVID-19 related findings dataset. *arXiv* **2020**, arXiv:2005.06465.